Journal of Materials Research and Technology 37 (2025) 3549–3562

Contents lists available at ScienceDirect

Journal of Materials Research and Technology

journal homepage: www.elsevier.com/locate/jmrt

Determination of Young's modulus in aluminum alloys: Role of precipitates, dispersoids, and intermetallics

H.W. Doty [a], J. Hernandez-Sandoval [b], H.R. Ammar [c], V. Songmene [d], F.H. Samuel [e,*]

[a] Materials Technology, General Motors Global Technology Center, Warren, MI, 48092, USA
[b] Facultad de Ingeniería Mecánica y Eléctrica, Universidad Autónoma de Nuevo León, San Nicolás de los Garza, Nuevo León, México
[c] Department of Mechanical Engineering, College of Engineering, Qassim University, Buraydah, 51452, Saudi Arabia
[d] Department of Mechanical Engineering, École de Technologie Supérieure, Montreal, Canada
[e] Université du Québec à Chicoutimi, Québec, Canada

ARTICLE INFO

Keywords:
Aluminum alloys
Young's modulus
Metal matrix composites
Tensile testing

ABSTRACT

The present work was performed on Al–Si–Mg–Cu and Al–Si–Mg alloys containing measured amounts of Ni (0.4 wt% and 4 wt%), Bi (1.0 wt%), Ca (0.5 wt%), Sr (0.015 wt%), 10 vol%SiC(p), and 20 vol%SiC(p). After solutionizing treatment, tensile bars (ASTM B108) were aged in the temperature range of 155 °C–350 °C for up to 100 h. The results of 700 tensile bars show that although the value of E is the Σ = E1+E2+ E3 +——, where E is a function of interparticle spacing and particle volume fraction of each type of precipitate, E can not be determined using a simple empirical formula due to interference of other factors such as porosity, inclusions, particle/matrix surface reaction, and precision of measuring each of the involved parameters. Considering alloying elements, the addition of a sufficient amount of Ni (Ni/Cu > 1), in the T6 condition, produces the highest E value, about 92 GPa (Al_2Cu, Al_3Ni, Al_3NiCu precipitates). Modification of the eutectic Si particles has a moderate improvement in E about precipitation hardening (about 12 %). The highest E value was obtained using metal matrix composites (359 alloy + 20 vol% SiC(p)) in the T6 condition, approximately 42 % improvement over that achieved using the base alloy, at 110 GPa.

1. Introduction

Various heat treatments can be performed on aluminum alloys. One of these, structural hardening, improves mechanical properties. To have an aluminum alloy that can undergo structural hardening, the alloying element in solution must have a higher solubility at high temperature than at low temperature. The solubility of copper is about 4.5 %, while at low temperatures, the solubility of the alloy is almost zero. Thus, upon cooling, the element in solution in the aluminum matrix can supersaturate the matrix during solidification [1–4].

Solution heating consists of heating the aluminum within a temperature range that will allow the dissolution of the alloying elements (Cu, Mg, Si, Zn), which participate in structural hardening. The solution time depends on the part size, the alloy, the manufacturing process, and the type of part, which influences the microstructure of the part. These factors determine the amount of additive element in solution, as well as the size and distribution of the precipitates [5,6].

Aging allows the alloy to increase its mechanical properties. There are three types of aging: natural, refrigeration, and artificial. The first, natural aging, consists of a partial return to equilibrium of the alloy by allowing the alloy elements in solution to precipitate at room temperature. The result is a part that will have the desired mechanical properties after a few days. For the second, artificial aging, precipitation is done in a furnace at a controlled time and temperature at the bottom of the solvus line. During aging, the Guinier-Preston (GP) zones appear first, followed by coherent precipitates. Incoherent precipitates are the last to appear and correspond to a decrease in the hardness of the alloy. Incoherent precipitates can also be called equilibrium precipitates [7–9].

The Guinier-Preston (GP) zones and coherent phases hinder dislocations' movement, generating significant stress and strain fields in their surroundings. To pass through the coherent precipitates, the dislocations shear them, hence the stress increases to cause deformation. If aging continued, stable equilibrium precipitates formed, which are incoherent with the matrix. With the lack of coherence that appears and the greater distance between the precipitates, the mode of movement of

* Corresponding author.
E-mail address: fhsamuel@uqac.ca (F.H. Samuel).

https://doi.org/10.1016/j.jmrt.2025.06.186
Received 19 April 2025; Received in revised form 22 June 2025; Accepted 25 June 2025
Available online 30 June 2025

the dislocations through the precipitate changes. They bypass the precipitates by an Orowan mechanism [10,11]. The dislocation, when it moves and crosses the precipitates, bends and leaves a loop of dislocations around each precipitate. The force required to deform aluminum decreases as the precipitates grow larger and the distance between the precipitates increases.

Depending on the type of alloy, the nature of the precipitate that participates in hardening is different. In the case of an alloy with copper, the precipitate formed is $CuAl_2$, according to the following sequence [12–15]:

Element in solid solution → GP → θ'' → θ'→ θ

For an alloy containing magnesium and silicon, the formed phase is Mg_2Si, and it precipitates in the following sequence [14,15]:

Element in solid solution → GP → β'' → β'→β

Precipitates θ'', θ′, β'', and β' represent the intermediates which are consistent with the matrix. The θ and β precipitates are the equilibrium precipitates and have no consistency with the matrix. Too long a time or too high a temperature can cause over-aging, which reduces the mechanical properties.

Nickel (Ni), compared to copper (Cu) and magnesium (Mg), exhibits less effect on the mechanical properties of Al–Si alloys. Ni is usually added at 2–3 % to improve alloys' mechanical properties at elevated temperatures. However, there is no reliable factor to corroborate this view since for nickel compositions of 0.1 % and less, 1.1 % and 1.9 %, the ultimate tensile stress does not differ significantly from one nickel composition to another. Since the interparticle spacing of Al_3Ni compounds is substantial, around 50 μm, this spacing would not permit a noticeable dispersion strengthening [16–19].

Dispersoids are hard and brittle particles formed in the liquid state, consisting of one element within the other, acting as a second phase in the aluminum matrix, leading to dispersion strengthening, which enhances the alloy's mechanical properties. These dispersoids are small and large in number. They are not affected by the precipitate-free zones that occur during aging, and hence better distribution of stresses. In addition, dispersoids are barriers to dislocation movement, resulting in higher alloy strength. Another type of dispersoids is introducing insoluble hard particles into the molten metal, such as Al_3Sc, SiC, Al_2O_3, B4C, and TiC particles at various volume fractions. This process is termed as metal matrix composites [20–23].

Young's modulus, a measure of the alloy stiffness, typically ranges from 69 GPa to 94 GPa for Al–Si complex alloys. A specific value can vary depending on the alloy composition and the applied heat treatment, in particular age hardening process. Alloying elements such as Mg and Cu, the presence of primary silicon particles, and interconnected intermetallics have a major influence on the value of the Young's modulus. The present work was undertaken to deeply analyse the phases and precipitation involved in the present study; define the role of primary silicon particles and interconnected intermetallics elements in determining the value of E; and describing the appropriate method of measuring the Young's modulus employing the results analysis of a huge number of tensile bars (10 bars/experimental condition).

2. Experimental procedure

2.1. Al–Si cast alloys

In the present study, two basic Al–Si cast alloys were used, and their chemical compositions are listed in Table 1. The alloys were received as 13.5 kg. Each alloy was remelted in an electrical furnace (Fig. 1(a)) equipped with a degasser made of surface-treated graphite (Fig. 1(b and c)) attached to the machine by a hollow graphite tube, rotating at the speed of 135 rpm with pure Ar gas going into the melt through fine holes made in each fin reaching into the inner tube. To avoid a vortex, a baffle plate made of ceramic (10 cm wide) was attached to the inner surface of the melting SiC crucible. Measured amounts of Ni were added to the molten bath of the 354-alloy in the form of Al–10 %Sr, Al–5 %Ti–1 %B, and Al-25 wt%Ni master alloys, respectively. In the case of the B319 alloy, Bi and Ca were added to the molten alloy in the form of Al-5 % Bi and Al-10 % Ca master alloys. The chemical analysis was carried out using a Spectrolab Jr CCD Spark Analyzer (3 samples/heat). Table 2 summarizes the chemical compositions of all prepared alloys. At the end of degassing, the molten metal was poured into a metallic permanent mold preheated at 450 °C, Fig. 1(d) displays the test specimen dimensions, according to ASTM-B-108. Once the casting is solidified, the casting is hung upside-down for cooling to room temperature, avoiding any possible shape deformation of the tensile bars -Fig. 1(e). Fig. 1(f) depicts the uniformity of the grain size across the gage length (average grain size ~20–25 μm).

Table 1
Chemical compositions of the two base alloys.

Alloy Code	Element (wt.%)							
	Si	Fe	Cu	Mn	Mg	Sr	Ti	Al
A354.1	9.1	0.12	1.8	0.0085	0.62	0.018	0.21	Bal
B319.2	6.14	0.11	3.65	0.0005	0.048	0.015	0.15	Bal

2.2. metal matrix composites

Table 3 exhibits the chemical compositions of the three alloys used in this section: 359-alloy + two Metal Matrix Composites containing 10 and 20 % in volume of SiC particulates. Hydrogen content in the composite melts was controlled by taking precautionary measures as preheating. Instead, a stirrer was made of surface-treated graphite with curved blades as shown in Fig. 1(c). Fig. 1(g) represents the simulation of the temperature and speed vectors of liquid 359-alloy using a special Fluent software. Both the temperature and the speed are almost uniform around the degassing system, with zero velocity near the surface due to the presence of the refractory baffle, whereas it is approximately 1.8 m/s within the melt. Considering the particulates' motion in the molten composites, Fig. 1(h) indicates that the SiC particles are uniformly distributed within the melt, from bottom to top direction inside the crucible. In addition, the arrows reveal that the particle's motion is from left to right.

All tensile bars were heat-treated before testing. The solutionizing temperature for 319 and 354 alloys was 510 °C, whereas the temperature for the 395, F3S.10S, and F3S.20S alloys was 540 °C. The solutionizing time in all cases was 8 h, followed by questioning in warm water (60 °C)-termed SHT. Artificial aging was carried out in blue M air forced ovens in the temperature range of 155 °C–250 °C for times of up to 200 h. For each condition, an average of five (5) bars was considered. Thereafter, tensile bars were pulled to fracture using a servo-hydraulic MTS tensile testing machine at a strain rate of 4×10^{-4}/s. An extensometer was attached to the gauge length to record the amount of deformation before fracture. Fig. 1(i) demonstrates the position of the test bar inside the grips. A laser beam was used to check the alignment between the test bar and the loading direction.

3. Results and discussion

3.1. Microstructural characterization and fractography

Fig. 2(a) depicts the microstructure of the base A354 alloy (coded A) in the as-cast condition, consisting of Al, β-Al_5FeSi, Al_2Cu, Q-$Al_5Cu_2Mg_8Si_6$ phases as determined using a wavelength dispersive spectrometer (WDS) system. Upon artificial aging at 155 °C/100 h (Fig. 2(b)), the microstructure reveals a high density of fine Cu-rich phase particles. Enlarging a portion of this micrograph (inset micrograph-upper right corner) displays the inter-particle distance of

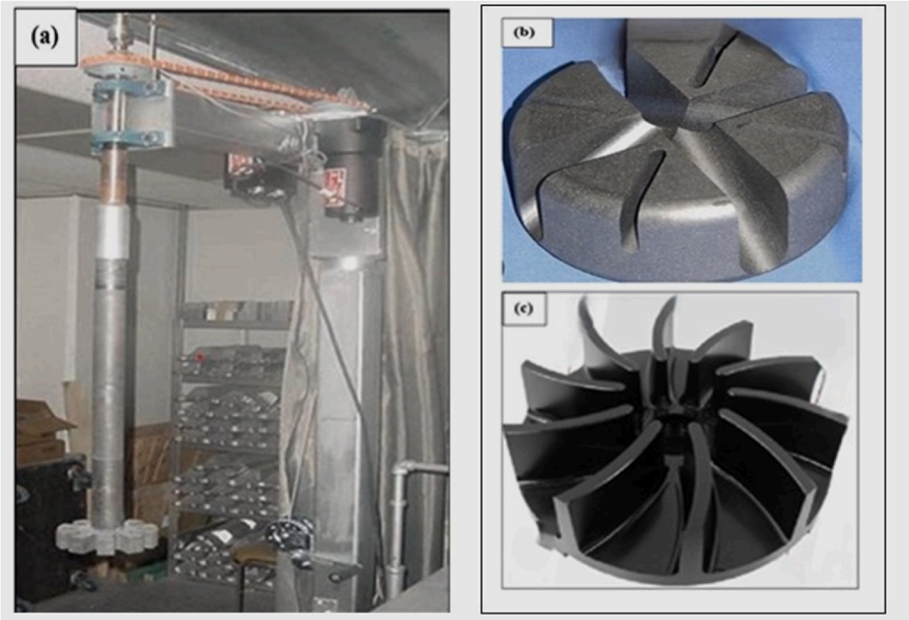

Fig. 1. (a) View of the used degassing system, (b) degassing graphite impeller, and (c) graphite stirring impeller.

Table 2(a)
Compositions of the 354-alloy series.

Alloy code	Composition
A	Base alloy 354
E	Alloy A + 0.4 wt%Ni
G	Alloy A + 4 wt%Ni

Table 2(b)
Compositions of the 359-alloy series.

Alloy code	Composition
W0	Base alloy B319.2
W9b	W0 + 900 ppm Bi
W4c	W0 + 400 ppm Ca

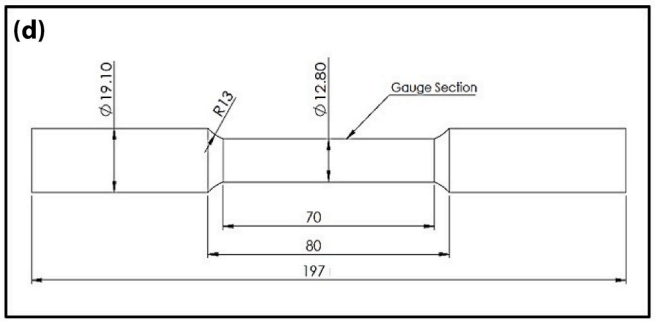

Fig. 1(d). Dimensions of the cast tensile bar in mm, according to ASTM-B-108.

Fig. 1(e). Placing the casting during the cooling stage.

about 40 nm on average. Such narrow interparticle distances will restrict the motion of dislocations [24–28] as shown in the bright field electron micrograph, revealing a particle that is tangled with dislocations (inset micrograph-lower corner). The microstructure of the same alloy following T7 tempering (250 °C/100 h) is displayed in Fig. 2(c), exhibiting coarsening of the particles shown in Fig. 2(b) with a marked increase in the interparticle distance to 200 nm. The Cu distribution in (c) is displayed in Fig. 2(d). Aging at a higher temperature, i.e., 350 °C for 100 h, resulted in a relatively spherical shape with almost equal interparticle distances (Fig. 2(e)). Fig. 2(f) reveals X-ray image of Cu distribution in (e).

The effect of adding Ni to the microstructure details of alloy G is highlighted in Fig. 3. The use of 0.4 wt% Ni is not enough to produce major intermetallics as shown in Fig. 3(a). Increasing the Ni concentration to 4 wt% resulted in the precipitation of a large number of insoluble Ni-rich intermetallics (about 9.7 vol%, using special software mounted on the electron probe microanalyzer type JEOL JXA-8900L employed in this study). An important observation to consider is that Ni has no affinity to react with Mg. Hence, part of the hardening following the T6 temper is due to precipitation of Mg_2Si ultra-fine phase particles. Fig. 3(b) shows alloy G in the as-cast condition, where the observed phases are indicated as follows: 1-Al-Al_3Ni eutectic, 2-AlNi-FeSi, 3-AlNiCu, and 4-Mg_2Si phases. Fig. 3(c) reveals the precipitation of Al_3Ni phase particles (about 2 μm in diameter) in the T7 condition (250 °C/200 h). The fracture surface of alloy G displayed in Fig. 3(d) of alloy G in the SHT condition reveals the presence of a new phase having the shape of a fishing net (area 1) with a composition close to Al_9NiCu in the neighbourhood of Al_3Ni phase particles (area 2). Most of the Ni-rich phases were insoluble at 510 °C/8 h.

(f)

Fig. 1(f). Grain size across the gauge length-inset shows the grain structure at high magnification.

Table 3
Chemical compositions of the used composites.

Alloy Code	Element (wt.%)								
	Si	Fe	Cu	Mn	Mg	Sr	Ti	$SiC_{(P)}$	Al
A395.1	9.5	0.2	0.2	0.0005	0.65	0.013	0.12	–	Bal
F3S.10S	9.5	0.2	0.2	0.0005	0.65	0.013	0.12	10 vol%	Bal
F3S.20S	9.5	0.2	0.2	0.0005	0.65	0.013	0.12	20 vol%	Bal

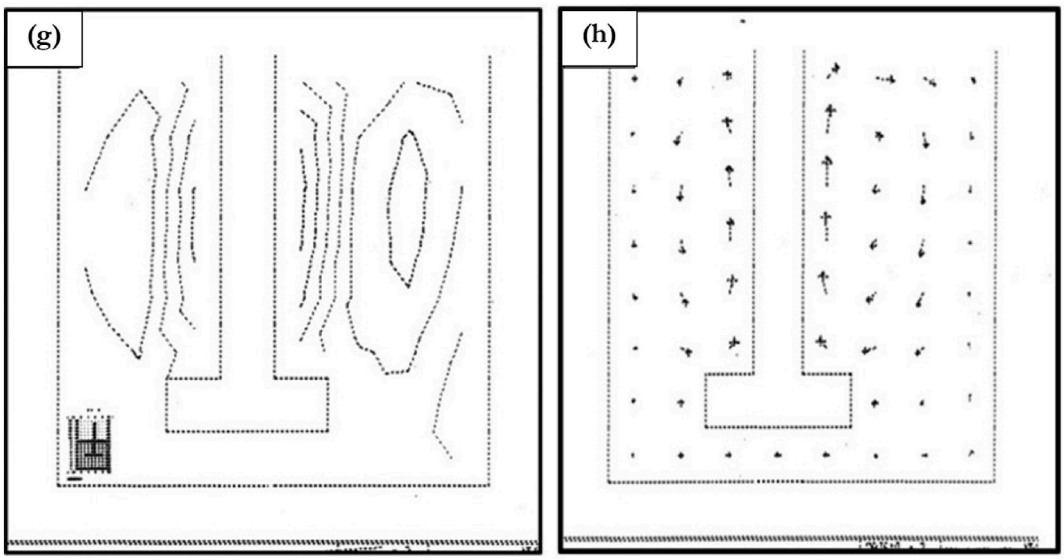

Fig. 1 (g). Temperature and speed in the liquid 359 alloy, (h) motion of the particulates in the molten composites.

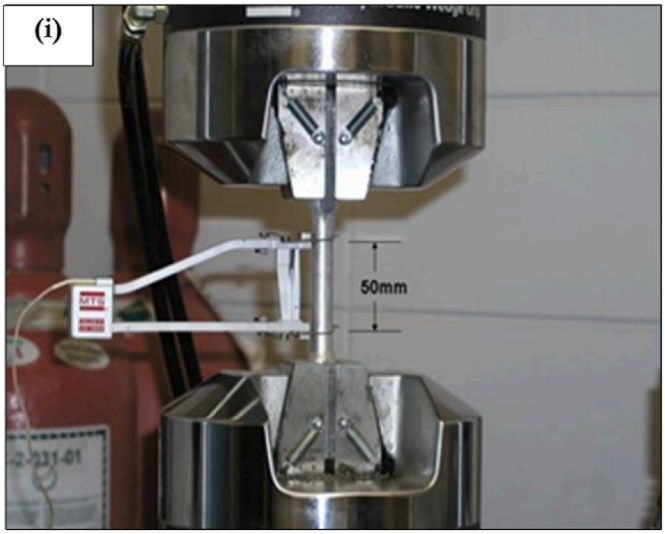

Fig. 1. (i) Positions of the tensile bar and extensometer.

Fig. 4 illustrates the demodification effect of Bi and Ca when added to Sr-modified alloys (i.e, B319 alloy in the present work). The results show that either the addition of 900 ppm Bi or 400 ppm Ca causes complete demodification of the alloy (see inset micrographs). It should be highlighted that the high levels of Bi and Ca were applied to evaluate their impact on the solidification of Al–Si–Cu/Sr-modified alloys. Furthermore, high levels of Bi and Ca are easily controlled/reproduced in the experimentations [28]. Fig. 4(a) displays an optical microstructure of B319.2 base alloy (W0), while Fig. 4(b) shows the microstructure of the base alloy with Bi addition (W0+900 ppm Bi (W9bc)). Fig. 4(c) reveals an X-ray electron image of Bi distribution, Fig. 4(d) reveals the microstructure of W0 + 400 ppm Ca (W5cc) alloy, and Fig. 4(e) shows the fracture surface of W4c alloy.

According to Ref. [29], Al_2Ca (a gray plate-like phase), Al_4Ca (ultra-fine eutectic colonies) are the main intermetallic phases in Al–Ca master alloys. The Al–Ca master alloys have a relatively low density (about 2.33 g/cm^3) compared to the matrix density (~2.7 g/cm^3) [30]. Fig. 4(e) represents the fracture surface of alloy 4(d), revealing the precipitation of undecomposed AlCa phase particles in the form of long rods surrounded by fractured α-AlFeSi and Q-AlMgCuSi phases, which is different from the two identified AlCa phases. In a previous study, the

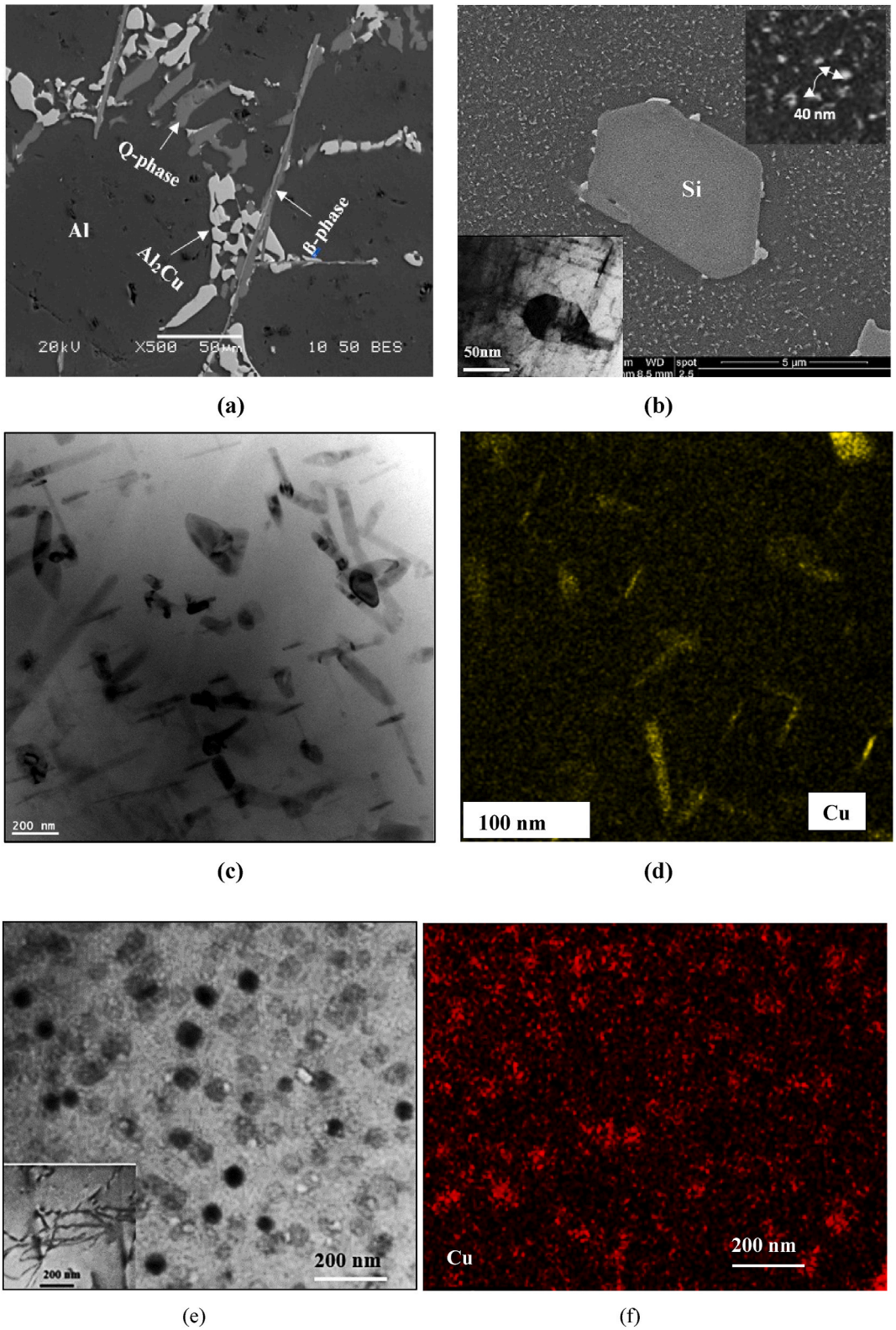

Fig. 2. (a) Backscattered electron image A alloy in the as cast condition, (b) alloy A in the T6 condition (155 °C/100h)-FESEM, (c) alloy A in the T7 (250 °C/100 h) -bright field image, STEM, (d) Cu distribution in (c), (e) 350 °C/100 h, STEM, (f) X-ray image of Cu distribution in (e).

authors interpreted the Ca–Sr and Bi–Sr interactions. While Ca has no poisoning effect in terms of demodification (Fig. 4(d)), the addition of Bi has an affinity to interact with Sr and Mg forming complex phases mainly BiSr, Bi_2Sr_3, Mg_2Bi_2 [31], reducing the available Sr amount for eutectic modification as shown in Fig. 4(b). The maximum solubility of Bi in solid aluminum is very limited (about 0.2 %). Thus, for 0.9 % Bi, Bi precipitation in the W9b alloy in the solid state is well-distributed in the form of small particles as displayed in Fig. 4(c).

The advantage of using 359-alloy as a base instead of the 356-alloy is that the high Si in the A395 alloy improves the alloy fluidity [32,33],

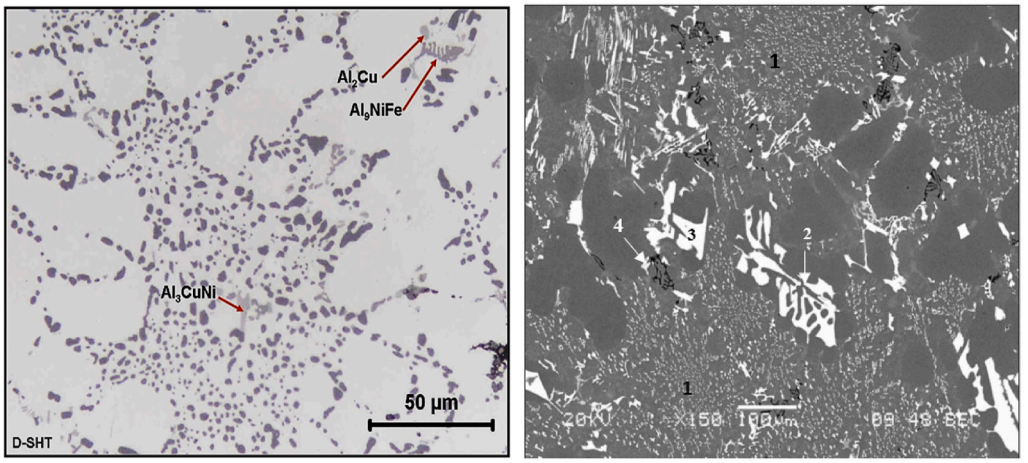

(a) (b)

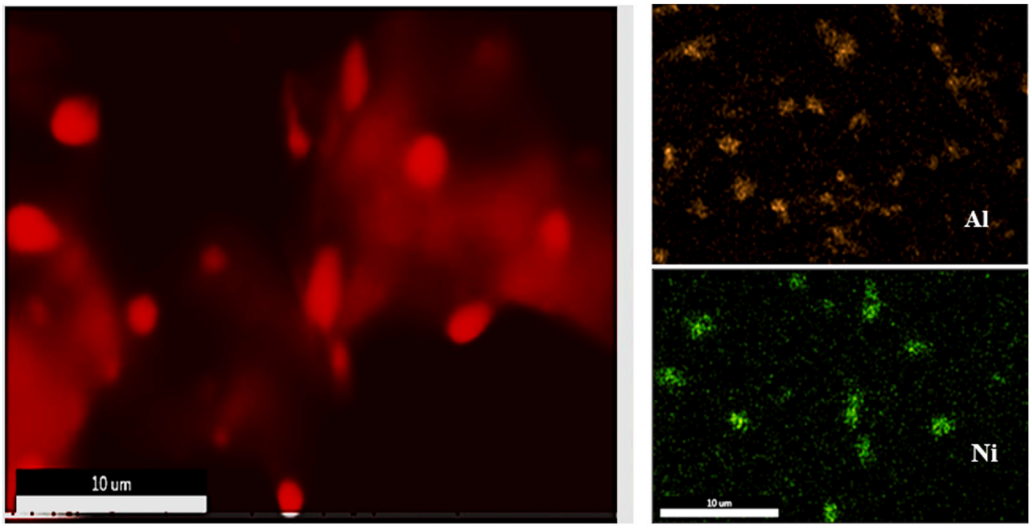

(c)

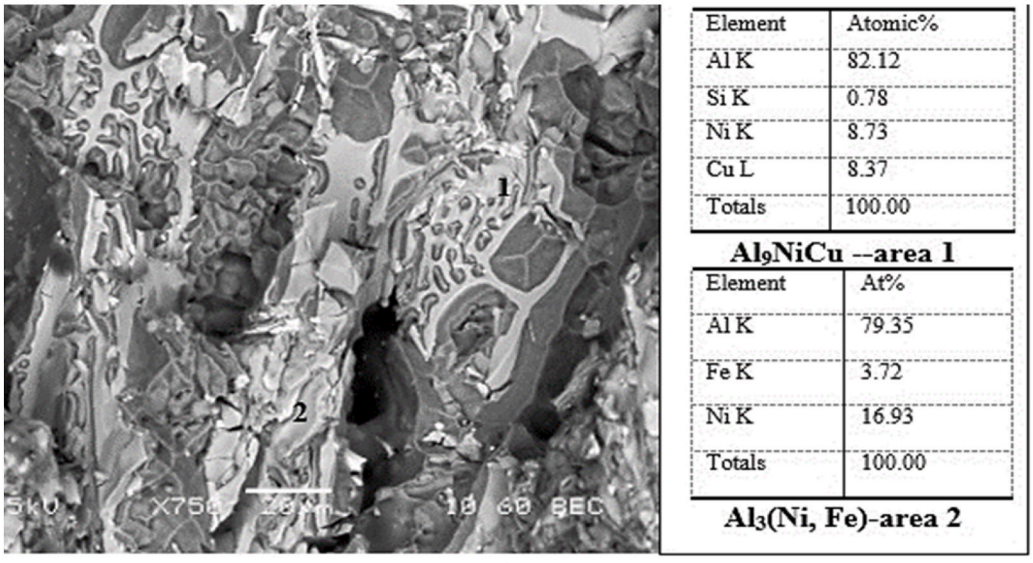

Element	Atomic%
Al K	82.12
Si K	0.78
Ni K	8.73
Cu L	8.37
Totals	100.00

Al_9NiCu --area 1

Element	At%
Al K	79.35
Fe K	3.72
Ni K	16.93
Totals	100.00

$Al_3(Ni, Fe)$-area 2

(d)

Fig. 3. (a) alloy E following solutionizing treatment, (b) alloy G in the as cast condition: 1-Al-Al_3Ni eutectic, 2-AlNiFeSi, 3-AlNiCu, and 4-Mg_2Si phases, (c) high angle annular dark field (HAADF) image for the alloy G after aging at 250 °C for 200 h (Al_3Ni particles), (d) fracture surface of alloy G in the SHT condition.

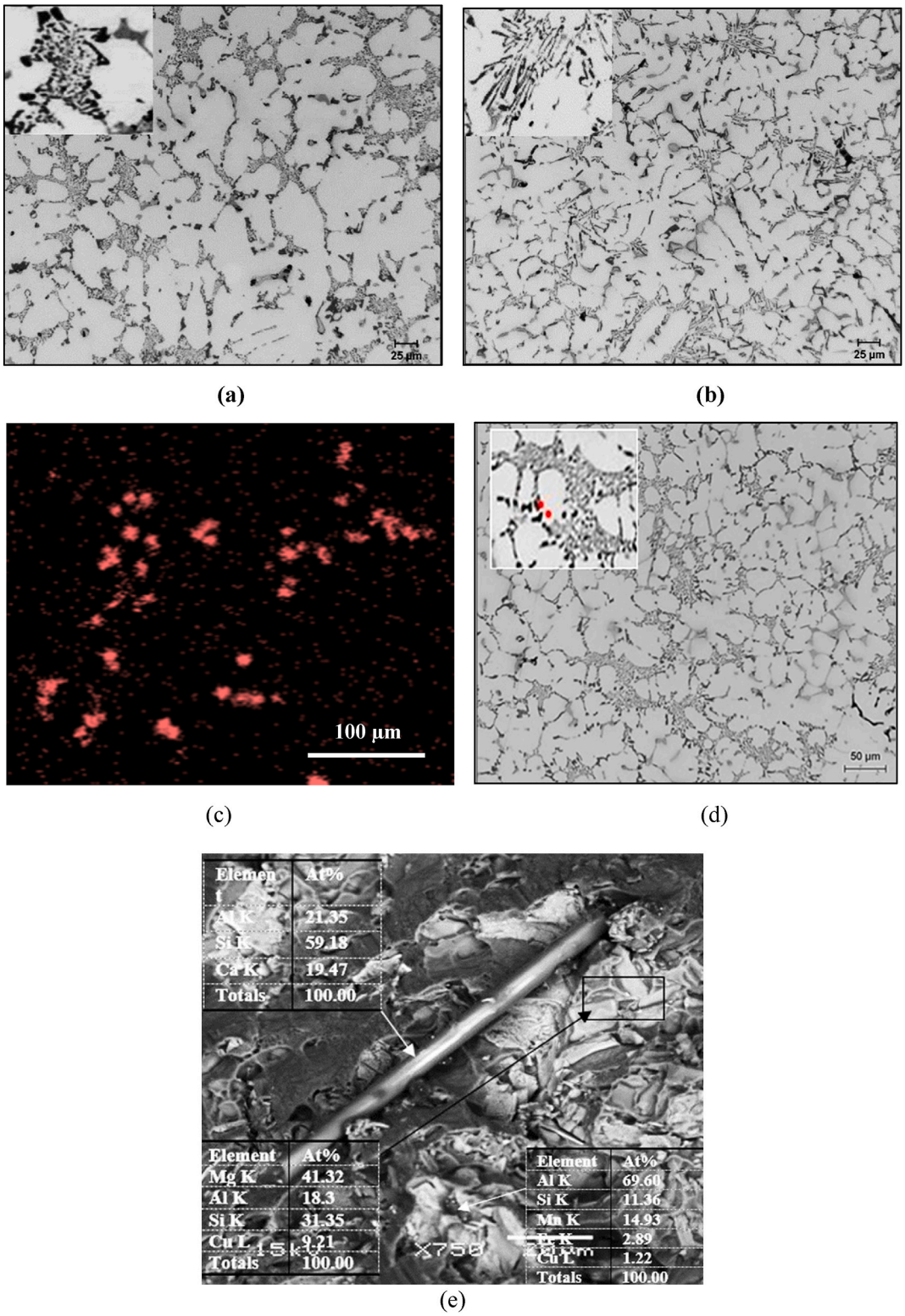

Fig. 4. Optical microstructure of B319.2 containing Bi and Ca**:** (a) base B319.2 alloy (W0), (b) W0+900 ppm Bi (W9bc), (c) X-ray electgron image of Bi distribution, (d) W0 + 400 ppm Ca (W5cc), (e) surface of alloy W4c.

leading to sounder castings compared to those obtained from the A356-MMC composites. In addition, high Si reduces the reaction between SiC and surrounding Al in the liquid state, resulting in the formation of a layer of Al_4C_3 carbide as black platelets bridging the SiC particles. The initiation of the Al_4C_3 reaction can be observed at the edges of the SiC particles. Since the A359 alloy contains Si and Mg with traces of Fe, solutionizing treatment will result in the dissolution of the Mg_2Si phase along with spheroidization of the eutectic Si particles as shown in Fig. 5(a). In this case, the average interparticle distance is approximately 20 µm. Comparison between Fig. 5(b) and (c) demonstrates the uniform distribution of the SiC particles throughout the matrix, absence of porosity or inclusions when the proper procedure is

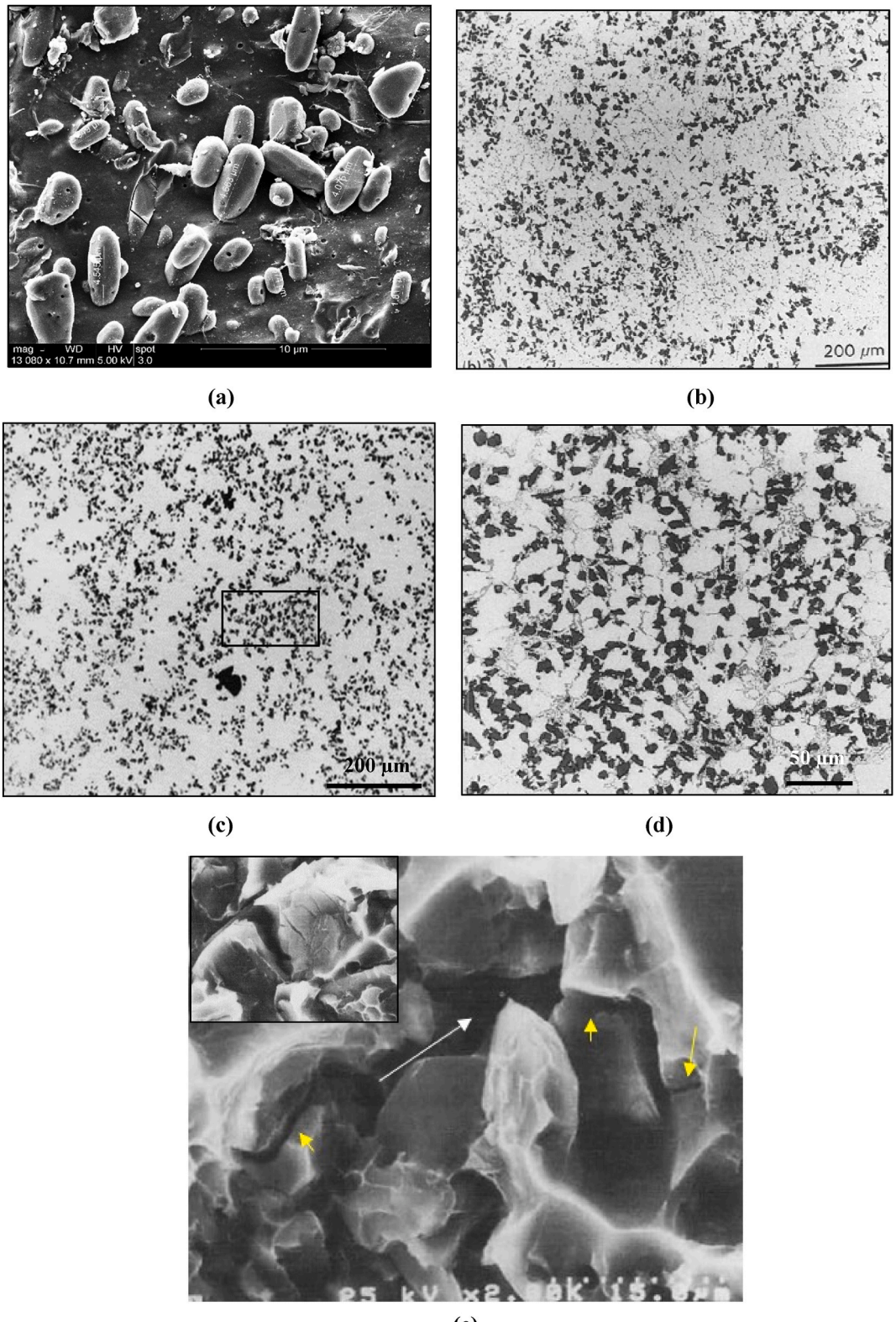

Fig. 5. Optical microstructure of: (a) A359 base alloy after solutionizing treatment, (b) F3S10S in the as cast condition, (c) F3S.20S in the as cast condition, (d) enlarged micrograpf of (c-rectangular area), (e) fracture surface of alloy F3S.20S in the T6 condition-white arrow indicates the crack propagation direction white yellow arrows point to cleaved particles.

followed during the melting and casting processes. In addition, Fig. 5(d) displays strong particle/matrix coherence and absence of chemical reactions between SiC and the surrounding Al matrix as inferred from the fracture of a SiC particle during tensile testing. Examining the fracture surface of test bars obtained in the T6 condition (F3S.20S), shown in Fig. 5(e), revealed that failure was mainly initiated and propagated in certain areas because of localized stresses. As a result, some of the SiC particles are cleaved due to strong particle/matrix bonding.

4. Tensile testing

Table 4 summarizes the tensile values obtained from alloy (A354.1) at different aging temperatures and times. The Young's modulus was reported as an average value of 5 tensile bars. The values listed in Table 4 are grouped for each aging temperature, where the first reading corresponds to low aging time and the last reading represents the highest aging time. Examples of the actual stress-strain curves are shown in Fig. 6 for different aging treatments.

Hafez and Farag [34] carried out a detailed study on the effect of particle size, interparticle spacing, and volume fraction of all particles in the matrix using Al–Cu and Al–Ni binary alloys with different Cu and Ni concentrations. All samples were annealed at 375 °C for 3 h. Based on the gathered data, the authors establish the following empirical formula:

$$E = 76.6 + 94.6\ V_d - 1.3d + 0.06\lambda \quad (1)$$

where E is Young's modulus, V_d is the volume fraction of all the dispersed phases, and d and λ are the average particle size and mean free path, respectively. The results display an improvement in the values of E with the increase in the volume fraction of existing dispersoids up to 20 %. The study was mainly based on optical microscopic examination. However, the authors did not take into consideration the interactions between the different alloying elements in complex alloys.

Table 4
Tensile properties of alloy A as a function of aging treatment.

Alloy Code	UTS (MPa)	YS (MPa)	Strain to fracture (%)	Young's Modulus (GPa)
A-AC	235	154	1.3	76-78 (±3 %)
A-SHT	304	161	5.6	70-72 (±3 %)
A1-155°C-2hrs	309	196	3.6	80-83 (±4 %)
A5-155°C-10hrs	367	308	1.4	
A13-155°C-100hrs	380	336	0.9	
A14-170°C-2hrs	348	261	2.6	82-86 (±4.5 %)
A18-170°C-10hrs	386	327	1.2	
A26-170°C-100hrs	338	300	1.2	
A27-190°C-2hrs	382	327	1.2	84-87 (±3.5 %)
A31-190°C-10hrs	360	320	0.9	
A39-190°C-100hrs	314	264	1.2	
A40-240°C-2hrs	312	263	0.9	84-76 (±2.8 %)
A44-240°C-10hrs	282	198	1.8	
A52-240°C-100hrs	240	137	2.8	
A53-300°C-2hrs	242	135	2.6	72-68 (±5 %)
A57-300°C-10hrs	223	116	3.0	
A65-300°C-100hrs	196	80	6.3	
A66-350°C-2hrs	221	101	4.5	63-58 (±5 %)
A70-350°C-10hrs	210	86	5.6	
A78-350°C-100hrs	198	81	6.3	

Based on the values reported in Table 4, solutionizing treatment led to a reduction in the value of E of the as-cast alloy (74 GPa) by about 8 % due to the increase in the alloy ductility coupled with a decrease in its strength. Upon aging at 155 °C–190 °C, with precipitation of ultra-fine Al_2Cu phase particles, the value of E increased by about 20 % compared to that of the as-cast alloy, reaching a maximum increase after aging at 190 °C for 100 h (88 GPa). In the case of T7 aged alloys, the value of E decreased continuously with the increase in both aging temperature and time reaching −20 % when the alloy with aged at 350 °C for 100 h (see Fig. 2(d)), concerning the initial value (72 GPa), and about 35 % concerning mT6 tempering. It should be noted that although all curves in each diagram seem to be branching from the same spot, the enlarged portion in Fig. 6(d) reveals that all curves were slightly separated at the start of testing, hence the observed variations. According to Nikitin et al. [35], increasing the Si content leads to an increase in the value of E. In addition, alloys prepared by quenching of the electromagnetically levitated melt had higher E values than those obtained with conventional casting, as shown in Fig. 6(e).

The effect of Ni addition on the level of E is presented in Fig. 7. All aging treatments used for alloy A were applied to alloy E. Apparently, the addition of 0.4 wt% Ni is not enough to produce marked changes in the value of E-Fig. 7(a). Although the Ni additions in the presence of Cu can significantly enhance the ultimate tensile strength (UTS) and yield strength of Al–Si alloys at elevated temperatures [35]. However, the addition of 4 wt% Ni resulted in reducing the alloy ductility due to the large insoluble intermetallics as displayed in Fig. 3, leading to a drop in the alloy strength as displayed in Fig. 7(b). Following the work of Hafez and Farag [34], the Young's modulus of the G alloy in the T6 condition recorded 92 GPa with a gain of about 27 % compared to the as-cast alloy. The Ni–Cu interactions in the G alloy (1.8 wt% Cu, 4 wt% Ni) lead to a reduction in the amount of Cu that will affect the hardening rate of the G alloy [36].

Based on the Al–Ni–Cu pseudo binary [37], K and δ phases will form. Precipitation of the delta phase (δ-Al_3CuNi) takes place during heat treatment and can influence the mechanical properties of the alloy, whereas the K-phase or (θ'-Al_2Cu) phase is a metastable precipitate that forms during age hardening, which is crucial for strengthening the Al–Cu alloys. Fig. 8 exhibits an example of Al_3NiCu phase particles observed in the G alloy. Thus, the reported increase in the E value may be interpreted in terms of the interparticle distances of all particles (dispersoids) that exist in the matrix.

Another aspect to be considered is the morphology of the Si eutectic particles, e.g., non-modified or Sr-modified. Fig. 9(a) and (b) display the stress-strain curves of the B319.2 alloy in the cast condition. In the case of a non-modified alloy (Fig. 9(a), eutectic Si is present in the form of sharp-edged platelets with a clear scatter in the level of stresses. In addition, the maximum % elongation is about 1.8 %. The calculated E value was found in the range 72–74 GPa. When the alloy is well modified, Fig. 9(b), all curves seem to be identical, giving a maximum % elongation of about 4 %, increasing the E level to about 79 GPa. This enhancement of the E value is directly related to the fragmentation of the eutectic Si particles as depicted in the inset micrograph.

Fig. 9(c) and (d) respectively represent the stress-strain curves of W9b and W5c alloys in the T6 condition (155 °C/8 h). Thus, the value of E will be determined based on the interparticle spacings of all precipitates and dispersoids available in the matrix (Al_2Cu, Si, and Bi phase particles and their total volume fractions). Therefore, the W9b alloy reported the highest E level in this series (87–89 GPa), followed by the W5c alloy (82–84 GPa).

The principal advantage of Al/Sic(p) composites is their high Young's modulus, which is needed for improved wear-resistance automotive brakes and other applications where lightweight materials with

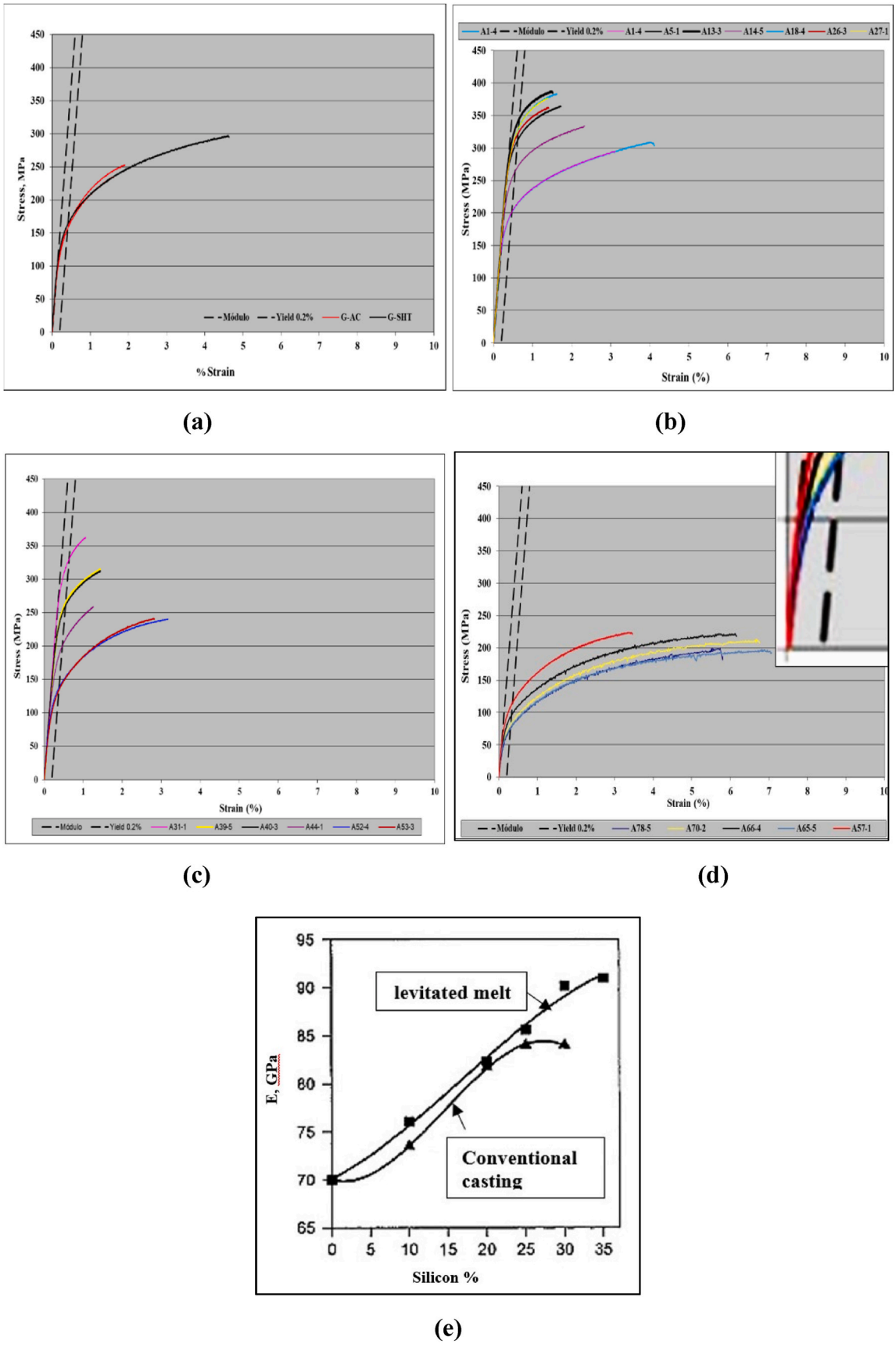

Fig. 6. Typical stress-strain curves obtained from alloy A at different heat treatment conditions: a) as cast and SHT, (b) T6 temper, (c) T7 temper, (d) T7 tempering at 350 °C (for details see Table 4), (e) variation of E value as a function of Si content and casting method [37].

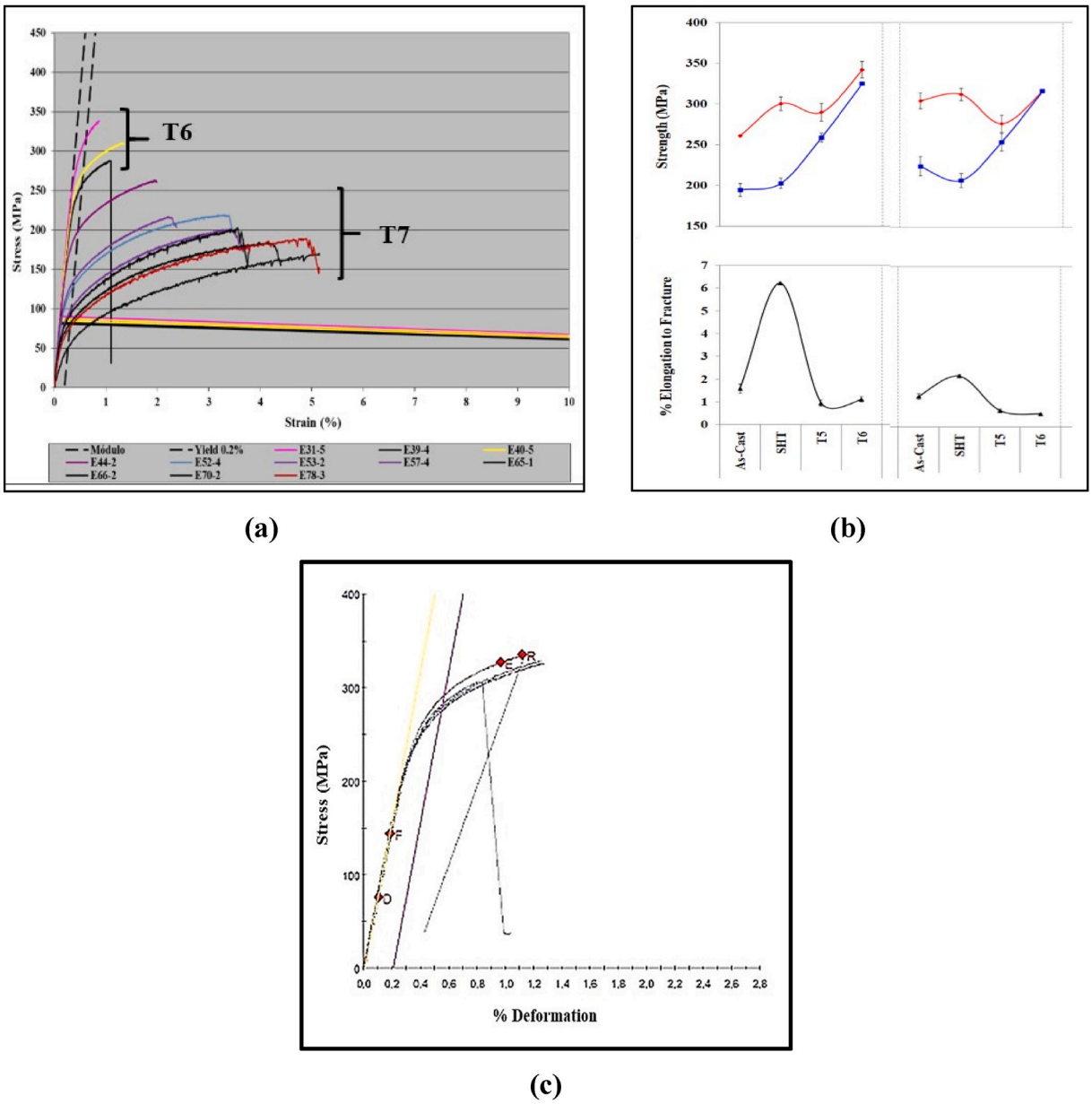

Fig. 7. (a) Typical stress-strain curves obtained from alloy E, tensile properties of alloy G, (c) stress-strain curves obtained from alloy G in the T6 condition.

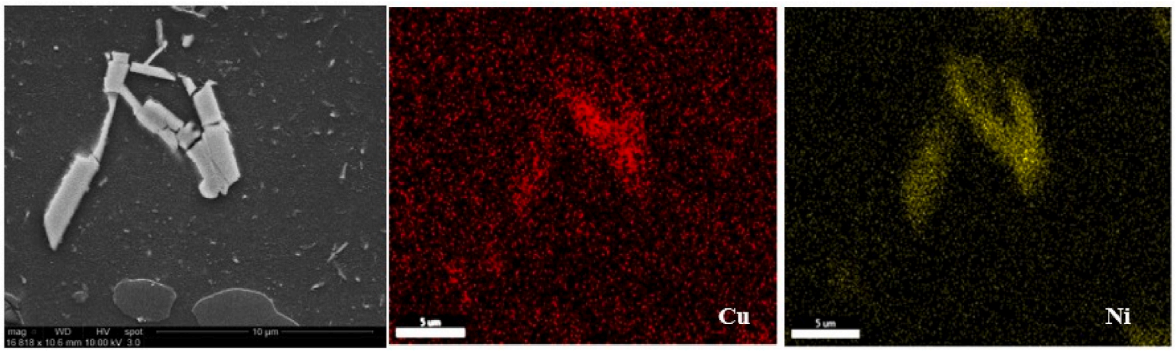

Fig. 8. Precipitation of Al_3NiCu phase particles in alloy G.

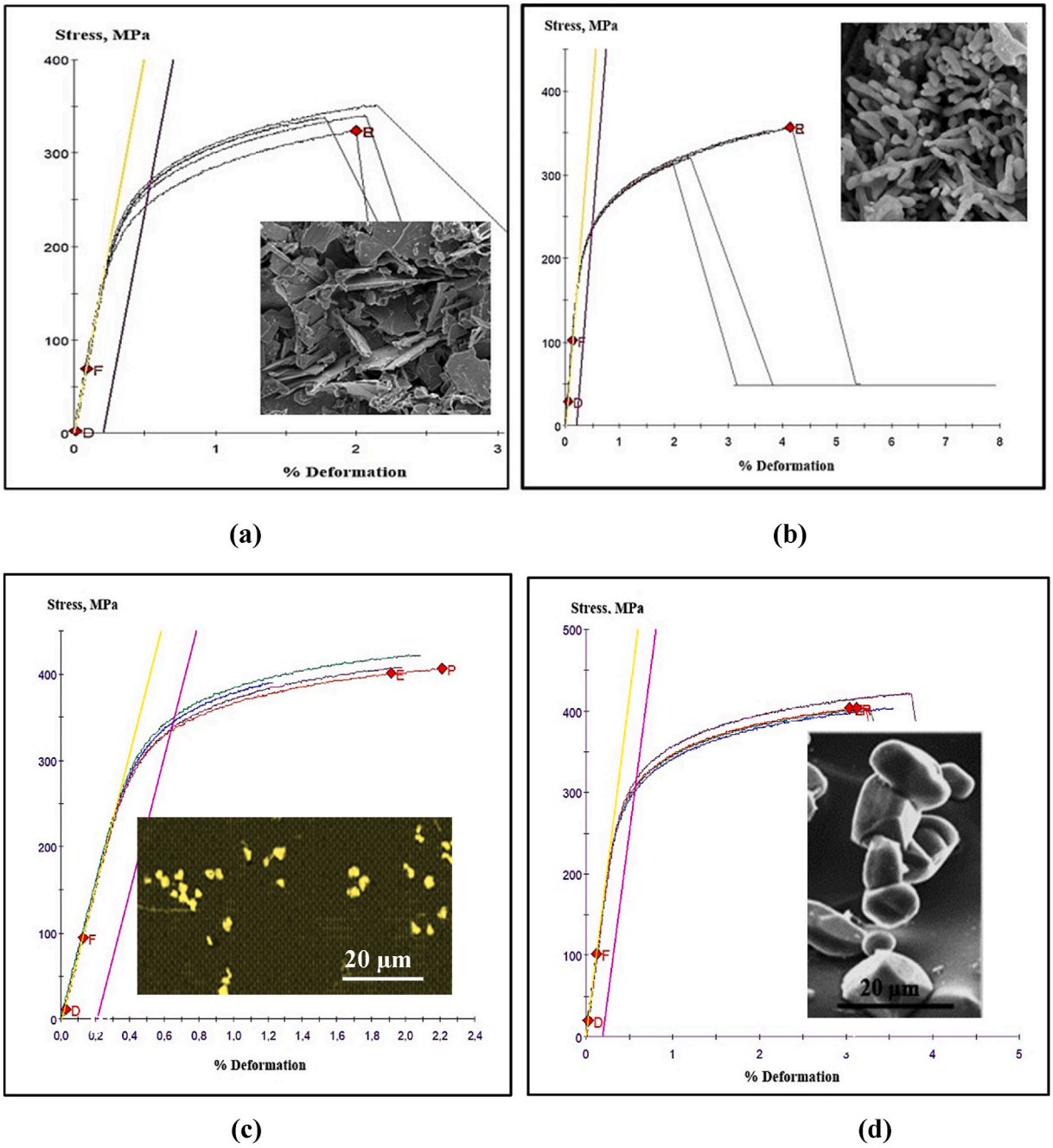

Fig. 9. Stress-strain curves of alloys: (a)W0-non modified, (b)W0 Sr-modified, (c)W9b, (d) W5c in the T6 condition. note the fragmentation of a Si fiber in the as-cast condition to a column composite of several small particles after the solutionizing treatment.

high stiffness values are required. Young's modulus of a given composite is directly attributed to the volume fraction of the added SiC(p), their sizes and distribution, as well as the interface between the SiC(p) and matrix. According to Ceschini et al. [38], because of the variations in the modulus of elasticity between the matrix and embedded particulates, the deformation occurs at the particle/matrix interface, inducing a high density of dislocations. It also enhances the modulus of elasticity value of the used composite. Alfonso et al. [39] and Tupaj et al. [40] proposed a rule to estimate the Young's modulus of the alloy matrix:

$$E_m = f\,E_f + (1-f)\,E_a \quad (2)$$

Where E_f and E_a are the Young's modulus of SiC(p) and matrix, and f is the reinforcement volume fraction. The results of Krizik et al. [41] on the methods of improving the Young's modules of Al–SiC composites show that, depending on the interface quality, the Young's modulus can vary over the range 88–120 GPa. On the other hand, SiC-matrix interface reactions will lead to a decrease in the composite Young's modulus.

Before tensile testing, selected tensile bars of F3S.20S were examined employing X-ray radiography for porosity or inclusions. Only a sample free of porosity was tested for determining the E value, as seen in Fig. 10, which displays the X-ray radiography of selected tensile bars of F3S.20S composite. Fig. 11 demonstrates the variation in the alloy/composite tensile properties as a function of the added volume fraction of SiC(p) treated in the T6 condition (155 °C/5 h). Although the addition of 20 vol % SiC(p) contributed to the alloy strength, and the ductility was reduced by about 82 %. From the slope of the curves, the approximate E levels (based on the average of 10 sound tensile bars) have been determined as 76, 92, and 107 GPa for 359, F3S.10S, and F3S.20S, respectively, with a

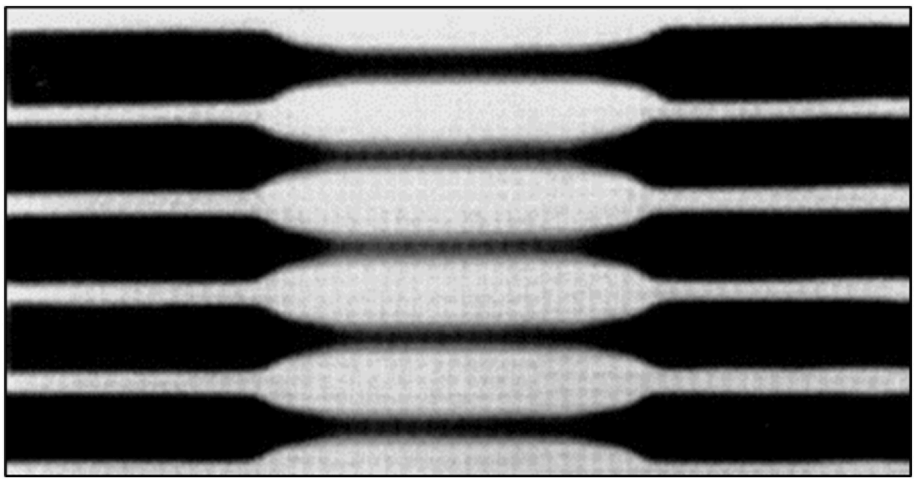

Fig. 10. X-ray radiography of some selected tensile bars of F3S.20S composite.

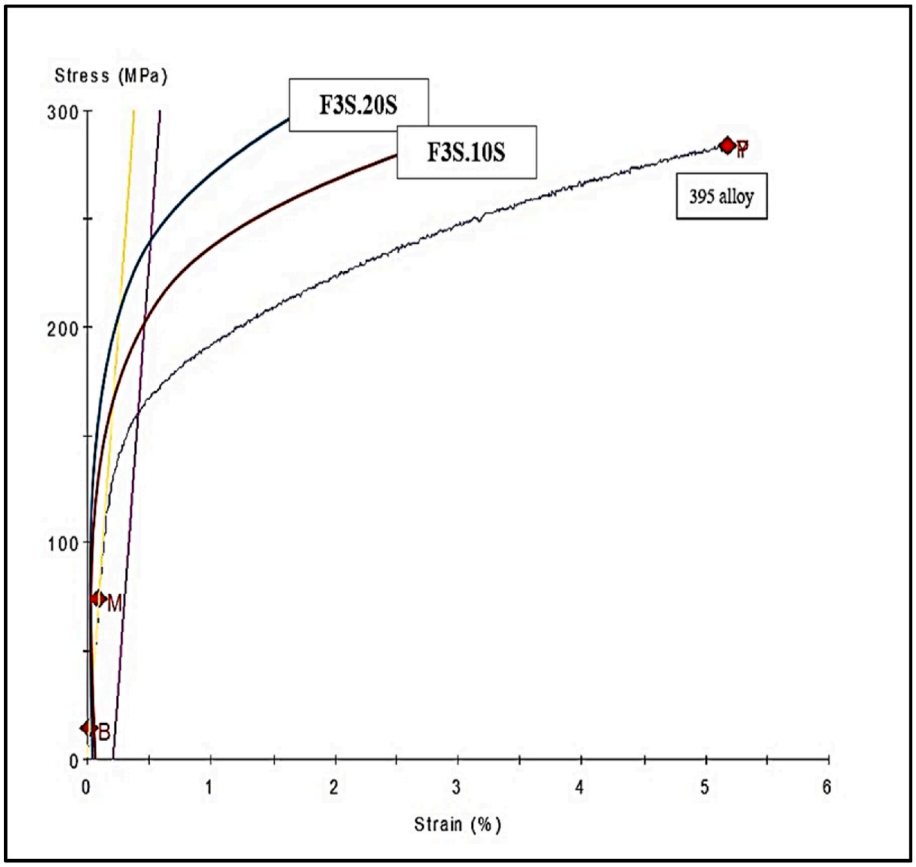

Fig. 11. Stress-strain curves of the present alloys in the T6 condition.

gain of ~42 %.

5. Conclusions

Based on the obtained results, the following conclusions may be drawn.

- Although the value of E is the Σ = E1+E2+ E3 +——, where E is a function of interparticle spacing and particle volume fraction of each type of precipitate, E can not be determined using a simple empirical formula due to interference of other factors such as porosity, inclusions, particle/matrix surface reaction, and precision of measuring each of the involved parameters.
- The ideal method of measuring E is the use of tensile testing under restricted conditions, i.e., perfect tensile bars and well well-aligned machine.
- Considering alloying elements, the addition of a sufficient amount of Ni (Ni/Cu > 1), in the T6 condition, produces the highest E value (Al_2Cu, Al_3Ni, Al_4NiCu precipitates).
- Modification of the eutectic Si particles has a moderate in improvement in E about precipitation hardening (about 12 %).

- The highest E value was obtained using metal matrix composites (359 alloy + 20 vol% SiC(p)) in the T6 condition-about 42 % improvement over that achieved using the base alloy.

Delaration of competing interest

There is no conflict of interest between the authors.

References

[1] Balarami Reddy T, Karthik P, Gopi Krishna M. Mechanical behavior of Al–Cu binary alloy system/Cu particulates reinforced metal-metal composites. Results Eng 2019;4:100046.

[2] Naga Swapna M. Mechanical characterization of Lm25/copper powder reinforced metallic composites. Int J Mech Eng Technol 2018:844–51.

[3] Zhang M, Liu T, He C, Ding J, Liu E, Shi C, Li J, Zhao N. Evolution of microstructure and properties of Al-Zn-Mg-Cu-Sc-Zr alloy during aging treatment. J Alloys Compd 2016;658:946–51.

[4] Lloyd DJ. Particle reinforced aluminium and magnesium matrix composites. Int Mater Rev 1994;39(1).

[5] Kang HJ, Jang HS, Oh S, Yoon P, Lee G, Park J, Kim E, Choi Y. Effects of solution treatment temperature and time on the porosities and mechanical properties of vacuum die-casted and T6 heat-treated Al–Si–Mg alloy. Vacuum 2021;193:110536.

[6] Shivkumar S, Ricci S, Keller C, Apelian D. Effect of solution treatment parameters on tensile properties of cast aluminum alloys. J Heat Treat 1990;8:63–70. https://doi.org/10.1007/BF02833067.

[7] Liu L, Hou Y, Ye T, Zhang L, Huang X, Gong Y, Liu C, Wu Y, Duan S. Effects of aging treatments on the age hardening behavior and microstructures in an Al-Mg-Si-Cu alloy. Metals 2024;14:238. https://doi.org/10.3390/met14020238.

[8] Engler O, Marioara CD, Aruga Y, Kozuka M, Myhr OR. Effect of natural ageing or pre-ageing on the evolution of precipitate structure and strength during age hardening of Al–Mg–Si alloy AA 6016. Mater Sci Eng, A 2019;759:520–9.

[9] Sunde JK, Marioara CD, Holmestad R. The effect of low Cu additions on precipitate crystal structures in overaged Al-Mg-Si(-Cu) alloys. Mater Char 2020;160:110087.

[10] Peng S, Wang Z, Li J, Fang Q, Wei Y. Beyond Orowan hardening: mapping the four distinct mechanisms associated with dislocation-precipitate interaction. Int J Plast 2023;169:103710.

[11] Bao H, Xu H, Li Y, Bai H, Ma F. The interaction mechanisms between dislocations and nano-precipitates in CuFe alloys: a molecular dynamic simulation. Int J Plast 2022;155:103317.

[12] Esmaeili S, Lloyd DJ. Effect of composition on clustering reactions in AlMgSi (Cu) alloys. Scr Mater 2004;50(1):155–8.

[13] Sjölander E, Seifeddine S. Artificial ageing of Al–Si–Cu–Mg casting alloys. Mater Sci Eng, A 2011;528:7402–9.

[14] Hodžić E, Domitner J, Thum A, Sabet AS, Müllner N, Fragner W, Sommitsch C. Influence of natural aging on the formability of Al-Mg-Si alloy blanks. J Manuf Process 2023;94:228–39.

[15] Werinos M, Antrekowitsch H, Ebner T, Prillhofer R, Uggowitzer PJ, Pogatscher S. Hardening of Al–Mg–Si alloys: effect of trace elements and prolonged natural aging. Mater Des 2016;107:257–68.

[16] Vončina M, Balaško T, Petrič M, et al. Effect of the addition of Ni and Cu on solidification microstructure evolution of Al-5Si-0.5Mg alloys. Int J Metalcast 2024. https://doi.org/10.1007/s40962-024-01449-8.

[17] Ibrahim MF, Samuel AM, Doty HW, Samuel FH. Effect of aging conditions on precipitation hardening in Al–Si–Mg and Al–Si–Cu–Mg alloys. Int J Metalcast 2017;11:274–86. https://doi.org/10.1007/s40962-016-0057-z.

[18] Li GJ, Guo MX, Wang Y, et al. Effect of Ni addition on microstructure and mechanical properties of Al–Mg–Si–Cu–Zn alloys with a high Mg/Si ratio. Int J Miner Metall Mater 2019;26:740–51. https://doi.org/10.1007/s12613-019-1778-9.

[19] Ding L, Zhang X, Lu C, Wang C, Weng Y, Dong Q, Xu S, Cao L, Jia Z. Influence of the combined additions Mn, Cr or Ni on the formation of dispersoids and mechanical properties of Al–Mg–Si–Cu alloys. Mater Sci Eng, A 2024;892:145962.

[20] Liu FZ, Qin J, Li Z, Yu CB, Zhu X, Nagaumi H, Zhang B. Precipitation of dispersoids in Al–Mg–Si alloys with Cu addition. J Mater Res Technol 2021;14:3134–9.

[21] Lodgaard L, Ryum N. Precipitation of dispersoids containing Mn and/or Cr in Al–Mg–Si alloys. Mater Sci Eng, A 2000;283(1–2):144–52.

[22] Wang R, Jiang S, Chen BA, Zhu Z. Size effect in the Al_3Sc dispersoid-mediated precipitation and mechanical/electrical properties of Al–Mg–Si–Sc alloys. J Mater Sci Technol 2020;57:78–84.

[23] Hichem F, Rebai G. Study of dispersoid particles in two Al–Mg–Si aluminium alloys and their effects on the recrystallization. Appl Phys A 2015;119:285–9. https://doi.org/10.1007/s00339-014-8963-5.

[24] Teichmann K, Marioara CD, Andersen SJ, Marthinsen K. TEM study of β′ precipitate interaction mechanisms with dislocations and β′ interfaces with the aluminium matrix in Al–Mg–Si alloys. Mater Char 2013;75:1–7.

[25] Dash SS, Chen D. A review on processing–microstructure–property relationships of Al–Si alloys: recent advances in deformation behavior. Metals 2023;13(3):609. https://doi.org/10.3390/met13030609.

[26] Ringdalen I, Wenner S, Friis J, Marian J. Dislocation dynamics study of precipitate hardening in Al–Mg–Si alloys with input from experimental characterization. MRS Commun 2017;7(3):626–33. https://doi.org/10.1557/mrc.2017.78.

[27] Hasting HS, Frøseth AG, Andersen SJ, Vissers R, Walmsley JC, Marioara CD, Holmestad R. Composition of β″ precipitates in Al–Mg–Si alloys by atom probe tomography and first-principles calculations. J Appl Phys 2009;106:123527.

[28] El-Hadad S, Samuel AM, Samuel FH, Doty HW, Valtierra S. Role of Bi and Ca additions in controlling the microstructure of Sr-modified 319 alloys. In: Proceedings of the 10th international conference on aluminum alloys; 2007, July 11–14. Vancouver, BC, Canada.

[29] Kumari SSS, Pillai RM, Pai BC. Role of calcium in aluminium-based alloys and composites. Int Mater Rev 2005;50(4):216–38. https://doi.org/10.1179/174328005X14366.

[30] Zaldívar-Cadena AA, Flores-Valdés A. Prediction and identification of calcium-rich phases in Al–Si alloys by electron backscatter diffraction EBSD/SEM. Mater Char 2007;58:834–41.

[31] Farahany S, Idris MH, Ourdjini A. Effect of bismuth and strontium interaction on the microstructure development, mechanical properties and fractography of a secondary Al–Si–Cu–Fe–Zn alloy. Mater Sci Eng, A 2015;621:28–38.

[32] Haga T, Imamura S, Fuse H. Fluidity investigation of pure Al and Al–Si alloys. Materials 2021;14(18):5372. https://doi.org/10.3390/ma14185372.

[33] Flemings MC, Niyama E, Taylor HF. Fluidity of aluminum alloys: an experimental and qualitative evaluation. AFS Transactions 1961;69:566–76.

[34] Hafez HA, Farag MM. Effect of structure on the Young's modulus of Al–Cu–Ni alloys. J Mater Sci 1981;16:1223–32. https://doi.org/10.1007/BF01033836.

[35] Abdelaziz MH, Samuel AM, Doty HW, Valtierra S, Samuel FH. Effect of additives on the microstructure and tensile properties of Al–Si alloys. J Mater Res Technol 2019;8(2):2255–68.

[36] Kim JH, Jeun JH, Chun HJ, Lee YR, Yoo JT, Yoon JH, Lee HS. Effect of precipitates on mechanical properties of AA2195. J Alloys Compd 2016;669:187–98. https://doi.org/10.1016/j.jallcom.2016.01.229.

[37] Li P, Nikitin VI, Kandalova EG, Nikitin KV. Effect of melt overheating, cooling and solidification rates on Al–16wt.%Si alloy structure. Mater Sci Eng A 2002;332:371–4.

[38] Ceschini L, Dahle A, Gupta M, Jarfors AEW, Jayalakshmi S, Morri A, Rotundo F, Toschi S, Singh RA. Metal matrix nanocomposites: an overview. In: Aluminum and magnesium metal matrix nanocomposites. Springer; 2017. p. 1–17. https://doi.org/10.1007/978-981-10-2681-2_1.

[39] Alfonso I, Figueroa IA, Rodriguez-Iglesias V, Patino-Carachure C, Medina A, Bejar L, Pérez L. Estimation of elastic moduli of particulate-reinforced composites using finite element and modified Halpin–Tsai models. J Braz Soc Mech Sci Eng 2016;38:1317–24.

[40] Tupaj M, Orłowicz AW, Mróz M, Trytek A, Dolata AJ, Dziedzic A. A study on material properties of intermetallic phases in a multicomponent hypereutectic Al–Si alloy with the use of nanoindentation testing. Materials 2020;13(22):5612.

[41] Krizik Peter, Balog Martin, Matko Igor, Peter Svec Sr, Cavojsky Miroslav, Simancik Frantisek. The effect of a particle–matrix interface on the Young's modulus of Al–SiC composites. J Compos Mater 2016;50(1). https://doi.org/10.1177/0021998315571.